Chemical Science

ROYAL SOCIETY OF CHEMISTRY

EDGE ARTICLE

View Article Online
View Journal | View Issue

Cite this: *Chem. Sci.*, 2025, **16**, 15438

All publication charges for this article have been paid for by the Royal Society of Chemistry

Rational crystal engineering of conductive metal–organic frameworks for promising electrochemical energy storage†

Hongbo Tai, Xuan Zhang, Yang Rong and Zhiliang Liu *

3D conductive metal–organic frameworks (c-MOFs) have emerged as a promising candidate for advancing energy storage due to excellent inherent electrical conductivity, efficient ion diffusion through open channels and high-density active sites. However, the facile preparation of 3D c-MOFs remains a great challenge. In this study, we developed two new 3D nitrogen-rich Ni-based c-MOFs (Ni-BPE and Ni-BPA) *via* the reaction of Ni^{2+} ions, 2-(3,5-dicarboxyphenyl)-6-carboxybenzimidazole (H_3L) and 1,2-di(4-pyridyl) ethylene dipyridyl (BPE) or 1,2-di(pyridin-4-yl) ethyne (BPA). The nitrogen-rich ligands, featuring pyridyl and benzimidazole units, extend the π-conjugation system, contributing to the high conductivity of Ni-BPE. Furthermore, compared to flexible BPE with a carbon–carbon double bond, the rigid BPA with a carbon–carbon triple bond can endow MOFs with a stronger π-electron delocalization. Owing to the advantageous properties enabled by crystal engineering, Ni-BPA exhibited an excellent electrical conductivity ($\sigma = 5.64 \times 10^{-3}$ S m^{-1}), which is 40% higher than that of Ni-BPE, accelerating electrochemical redox kinetics. Theoretical calculations confirmed the effect of electronic structure modulation on conductivity. Correspondingly, Ni-BPA produced a high specific capacitance of 532.4 F g^{-1} (266.2 C g^{-1}) at 1 A g^{-1}, surpassing Ni-BPE by 52.1%. Notably, the Ni-BPA//AC device maintained excellent cycle stability with a capacitance retention of 91.9% and a high coulombic efficiency of 98.6% after 10 000 cycles.

Received 16th April 2025
Accepted 19th July 2025

DOI: 10.1039/d5sc02794b

rsc.li/chemical-science

Introduction

Metal–organic frameworks (MOFs), a class of crystalline porous materials with a long-range ordered structure, are self-assembled from metal ions/clusters with organic ligands, and generally possess unique characteristics of structural diversity, high specific surface area and facile crystal engineering.[1–5] As a result, advanced MOF-based materials are being applied in different fields like gas storage and separation,[6,7] electromagnetic wave absorption,[8,9] catalysis[10–12] and chemical sensing.[13–15] Recently, porous MOFs have been utilized as promising electrode materials for supercapacitors (SCs) owing to their built-in redox active sites for electrochemical reactions.[16–18] Nevertheless, because most organic ligands suffer from the insulating nature or the overlap between π-orbitals of linkers and d-orbitals of metal ions is poor, these MOFs typically possess insufficient electronic conductivity,[19–22] inevitably hindering direct application as electrode materials for SCs.

To meet this challenge, commonly, MOFs are either combined with conductive materials to obtain MOF composites or employed as precursors to obtain MOF-derived materials.[23–26] For example, Davarani *et al.* used Mn-based MOF as a sacrificial template to fabricate the MnTe@ZnMnTe@RGO composite through a complicated five-step reaction that integrates solvothermal growth, annealing and tellurization, which demonstrated outstanding electrochemical properties.[27] It is obvious that these processes necessitate intricate processing protocols and any inadvertent negligence may lead to both partial or complete pore blockage and framework collapse, losing the intrinsic structural advantages of MOFs.[28,29] Consequently, extensive efforts have been directed toward designing effective strategies to fabricate intrinsically conductive MOF-based electrodes with enhanced charge transport capabilities.

2D conductive MOFs (c-MOFs),[30–33] extended π-d conjugated structures which formed through planar organic ligands and transition-metal nodes, represent a positive breakthrough for the development of SC electrode materials. Electron long-range delocalization arising from the in-plane π-d conjugation architecture endows 2D c-MOFs with superior intrinsic conductivity, significantly improving the utilization of built-in redox active sites and upgrading electrochemical

Inner Mongolia Key Laboratory of Chemistry and Physics of Rare Earth Materials, College of Chemistry and Chemical Engineering, Inner Mongolia University, Hohhot, 010021, PR China. E-mail: cezlliu@imu.edu.cn

† Electronic supplementary information (ESI) available: Materials and instrumentation, and supplementary figures and tables. CCDC 2430968 and 2430967. For ESI and crystallographic data in CIF or other electronic format see DOI: https://doi.org/10.1039/d5sc02794b

performance. Nevertheless, owing to the closely stacked layers, 2D c-MOFs probably possess insufficient specific surface area and inadequate accessibility of ions into the pores, impeding electrochemical reaction.[34,35] Hence, 3D "pillared-layer" c-MOFs with expanded interlayer spacing and high specific surface areas may be more interesting.[36] On the other hand, nitrogen-rich MOFs, self-assembled from nitrogen-containing organic ligands and metal blocks, have emerged as one of the most promising candidates for supercapacitor electrodes.[37,38] Generally speaking, nitrogen-containing ligands typically possess stronger conjugated structures and superior electron delocalization capabilities. The lone pair electrons of nitrogen atoms could participate in forming extended π-conjugated systems, thereby reducing the band gap of materials and facilitating electron migration within the framework.[39,40] Notably, the preparation of nitrogen-rich 3D c-MOFs with high specific surface areas and the deep understanding of the structure–property relationship remain great challenges.

Given the molecular-level customizability of MOFs, crystal engineering centered on the rational design of organic linkers is one of the effective strategies for endowing targeted MOFs with specific properties.[41–45] For instance, by incorporating highly π-conjugated ligands or extending the π-conjugation of ligands, the intrinsic electrical conductivity of MOFs can be optimized.[46,47] Herein, we first prepared a "pillared-layer" 3D c-MOF (Ni-BPE) by using two kinds of conjugated nitrogen-rich ligands, 2-(3,5-dicarboxyphenyl)-6-carboxybenzimidazole (H_3L) and 1,2-di(4-pyridyl) ethylene dipyridyl (BPE). The extended π-conjugation system of H_3L and BPE facilitates electrons delocalization, thereby promoting efficient electron transfer in Ni-BPE. Meanwhile, the lengths of H_3L and BPE contribute significantly to increasing the size of open channels. Inspired by crystal engineering, we successfully synthesized isomorphic 3D c-MOF (Ni-BPA) by replacing flexible BPE with rigid BPA, an additional N-donor ligand featuring an ethynyl group that demonstrates increased delocalization strength. Encouragingly, Ni-BPA exhibited promising conductivity and improved specific capacitance.

Experimental

Sample synthesis

Synthesis of Ni-BPE. $\{[Ni(HL)(BPE)]\cdot DMF\cdot H_2O\}_n$. A mixture of $NiCl_2\cdot 6H_2O$ (0.4 mmol, 95.0 mg), H_3L (0.2 mmol, 65.0 mg), BPE (0.2 mmol, 36.5 mg), 30 mL H_2O and 30 mL DMF was added into a 100 mL Teflon-lined stainless steel vessel. Subsequently, the resulting solution was ultrasonicated for 30 minutes at room temperature and heated at 105 °C for 72 hours. After cooling to room temperature, green block crystals were gained through filtration and drying. Yield: ~67.0%. IR (KBr, cm^{-1}): 3439 (m), 2023 (w), 1651 (s), 1610 (s), 1408 (s), 1105 (s), 986 (w), 832 (w), 778 (w), 721 (w), 615 (m), 545 (m).

Synthesis of Ni-BPA. $\{[Ni(HL)(BPA)]\cdot DMF\}_n$. The synthesis of Ni-BPA is similar to that of Ni-BPE. Specifically, 19.0 mg $NiCl_2\cdot 6H_2O$ (0.08 mmol), 13.0 mg H_3L (0.04 mmol), 7.2 mg BPA (0.04 mmol), 2 mL H_2O and 2 mL DMF were added into a 23 mL Teflon-lined stainless steel vessel and ultrasonicated for 30 minutes at room temperature. Then, the reaction was continuously heated for 72 hours at 105 °C and cooled to room temperature. Ultimately, dark green block crystals were washed with DMF to harvest the pure samples. Yield: ~65.0%. IR (KBr, cm^{-1}): 3439 (m), 2023 (w), 1651 (s), 1610 (s), 1408 (s), 1105 (s), 986 (w), 832 (w), 778 (w), 721 (w), 615 (m), 556 (m).

The crystal structure determination

A Bruker APEX-II CCD X-ray single-crystal diffractometer with Ga Kα radiation ($\lambda = 1.34139$ Å) at 150.00 K was used to collect the single-crystal diffraction data of Ni-BPE and Ni-BPA. The crystal structures were solved by direct methods and refined with the SHELXL-2018 program, implemented within the Olex-2.[48] H atoms were placed in ideal positions in theory using a riding model while all non-hydrogen atoms were refined anisotropically. The crystal data and structural refinements were collected and are shown in Table S1† while the bond distances and bond angles are listed in Tables S2 and S3.† The CCDC numbers of Ni-BPE and Ni-BPA are 2430968 and 2430967, respectively.

Computational methods

All calculations used the projector augmented wave (PAW) method within density functional theory (DFT) as implemented in the VASP.[49] Electron exchange–correlation interactions were modeled using the GGA-PBE functional,[50] with spin polarization included. The Brillouin zone was sampled with a Γ-centered k-mesh ($2\pi \times 0.04$ $Å^{-1}$ for geometry optimization and $2\pi \times 0.02$ $Å^{-1}$ for the electronic structure). A 450 eV plane-wave cutoff was used, with convergence criteria of 0.02 eV $Å^{-1}$ for forces and 10^{-5} eV for energy. van der Waals interactions were included *via* the DFT-D3 method with Becke–Johnson damping.[51,52] Structures were visualized using VESTA.[53]

Results and discussion

Characterization

As shown in Scheme 1, a new 2-fold interpenetrated 3D Ni-based MOF, Ni-BPE, was first prepared *via* the coordination

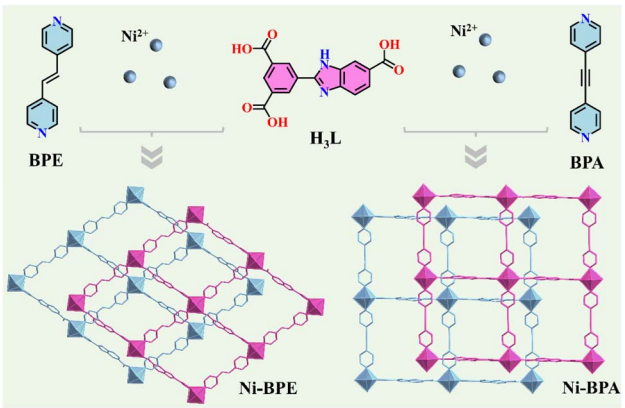

Scheme 1 Schematic illustration of Ni-BPE and Ni-BPA.

polymerization of Ni^{2+} ions and two kinds of nitrogen rich conjugated ligands with strong π-electron delocalization, H_3L and BPE. Owing to nitrogen-rich coordination and extended π-electron delocalization, Ni-BPE exhibits excellent conductivity. Through crystal engineering that involves replacing a flexible BPE ligand with a more conjugated rigid BPA linker featuring an ethynyl group, the new isomorphic Ni-BPA with a 2-fold interpenetrated structure has been successfully synthesized, meaningfully promoting conductivity and electrochemical performance.

Single-crystal diffraction analysis reveals that Ni-BPE and Ni-BPA crystallize in the triclinic space group $P\bar{1}$ (Table S1†). As shown in Fig. 1a and b, their unit cells all contain one crystallographically independent Ni(II) ion, one deprotonated HL^{2-}, and one dissociated DMF. Differently, Ni-BPE includes one BPE ligand with a vinyl group, while Ni-BPA contains one BPA ligand consisting of an ethynyl group. Ni-BPE also includes one lattice H_2O molecule. The H atoms on the three carboxyl groups and the N atoms at the 3-position on benzimidazole in compounds are ionized and protonated, respectively.[54] The Ni1 ion is bound by four carboxyl oxygen atoms (O1, O3 B, O4 B and O6 C) of three HL^{2-} ligands and two nitrogen atoms (N1 and N2 A) from two pyridine ligands, all exhibiting a six-coordinated {Ni(1)N_2O_4} distorted-octahedral configuration (Fig. 1c), where four O atoms form the equatorial plane and two N atoms occupy the two vertices. For Ni-BPE (Table S2†), the bond lengths between the Ni and O atoms are 2.028(2)–2.168(2) Å, and between the Ni and N atoms are 2.068(3)–2.069(3) Å. Additionally, the O–Ni–O bond angles fall within reasonable ranges of 61.50(8)–158.48(9)°. For Ni-BPA (Table S3†), the bond lengths of Ni–O and Ni–N are 2.018(18)–2.163(19) Å and 2.056(3)–2.065(3) Å, and the bond angles of O–Ni–O are 61.78(7)–158.21(8)°. The bond lengths and bond angles above are in accordance with those reported.[54]

Interestingly, as depicted in Fig. 1e, the HL^{2-} unit in Ni-MOFs all adopt μ^4-$\eta^2/\eta^1/\eta^1$ coordination mode, connecting with three Ni(II) ions to generate 2D metal-carboxylic layers (Fig. 1g). Subsequently, the adjacent 2D metal-carboxylic layers are connected by BPE or BPA pillars to yield a "pillared-layer" 3D framework with 1D 13.7 Å × 12.5 Å or 13.7 Å × 12.2 Å channels (Fig. 1h or i), in which pyridine ligands adopt μ^2-η^1/η^1 coordination modes (Fig. 1d or f). Ultimately, 2-fold interpenetrating architectures of Ni-BPE or Ni-BPA were observed owing to the large channel dimension (Fig. S1†), which could provide the possibility of excellent stability for frameworks. Notably, by using PLATON software, after the removal of solvent molecules, the theoretical porosities of Ni-BPE and Ni-BPA have been calculated to be 41.5% and 44.4%, respectively, proving their high theoretical porosities.

Further characterization studies were performed on the prepared samples to analyze their bulk properties and bonding information in detail. As depicted in Fig. 2a, the powder X-ray diffraction (PXRD) patterns reveal that the diffraction peaks of compounds match closely with those of the simulated PXRD pattern, proving their high phase purities and sharp peaks indicate high crystallinities. Furthermore, Fig. 2b shows the Fourier transform infrared (FTIR) spectrum of the as-synthesized samples recorded in the region from 4000 to 400 cm^{-1}. The signals at 1653 cm^{-1} and 1610 cm^{-1} are generated by asymmetric stretching vibration of $-COO^-$ ligands (ν_{as}(COO)) and peaks at around 1408 cm^{-1} correspond to the symmetric stretching vibration of $-COO^-$ groups (ν_s(COO)).

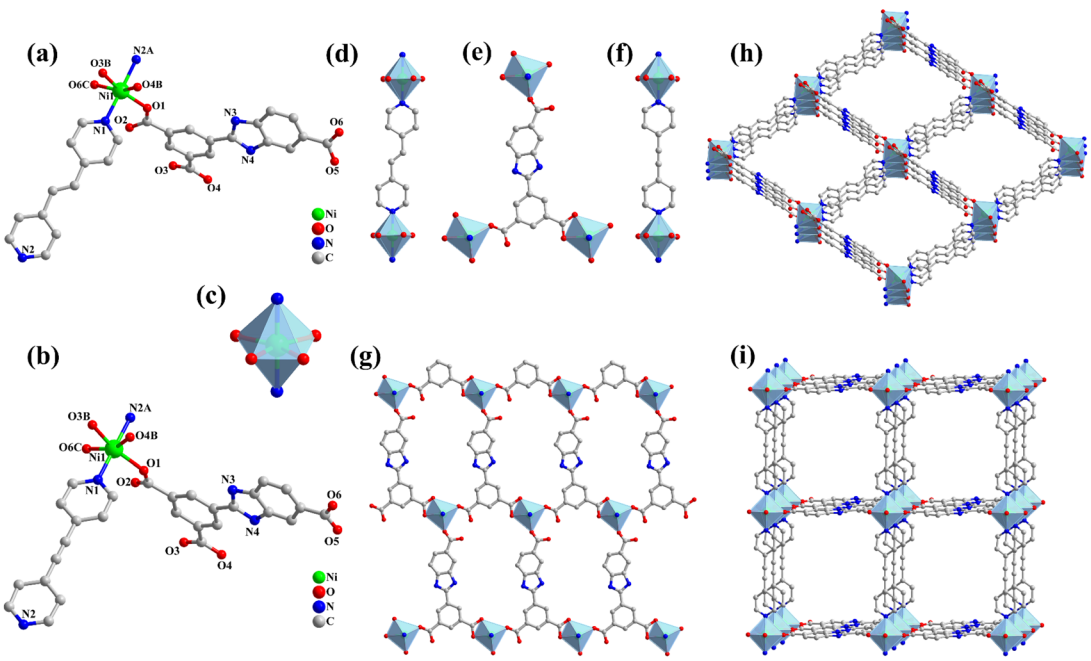

Fig. 1 Coordination structures of the Ni(II) ion (symmetry codes: (A) +*X*, −1 + *Y*, +*Z*; (B) 1 + *X*, +*Y*, +*Z*; (C) +*X*, +*Y*, −1 + *Z*) in Ni-BPE (a) and Ni-BPA (b). {Ni(1)N_2O_4} configuration (c). Coordination environment of BPE (d), H_3L (e), and BPA (f). 2D Ni-carboxylic layer (g). 3D framework of Ni-BPE (h) and Ni-BPA (i). Color codes for atoms: green, Ni; red, O; blue, N and gray, C.

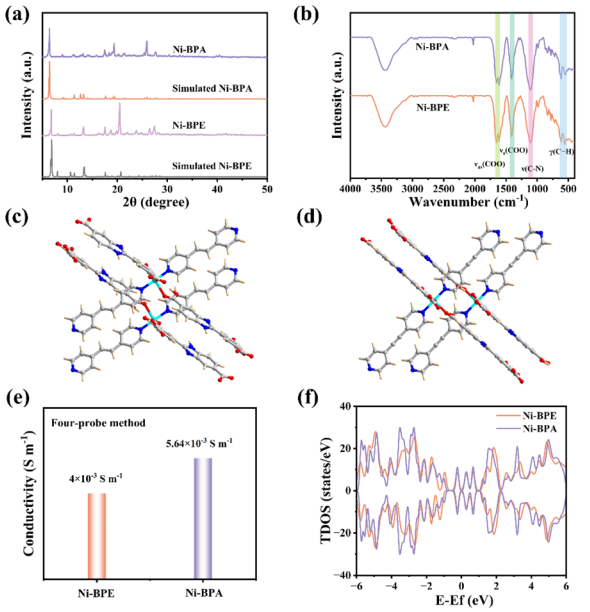

Fig. 2 (a) PXRD patterns. (b) FTIR spectra. Constructed models of Ni-BPE (c) and Ni-BPA (d) for calculation. The electrical conductivity at room temperature (e) and DOS (f) of the compounds.

Additionally, the intense bands observed at 1105 cm^{-1} arise from the stretching vibration of the C–N bonds (ν(C–N)) and the peaks at 545–615 cm^{-1} are attributed to out-of-plane bending of the C–H bonds (γ(C–H)). As shown in Fig. S2,† for Ni-BPE, before 250 °C, a weight loss of 13.8% is observed, corresponding to the release of one free DMF solvent molecule and one H_2O molecule in the framework (calculated 14.4%). Notably, the frame structure remains stable before 330 °C. For Ni-BPA, the weight loss (11.9%) occurring around 25–250 °C is attributed to the loss of one free DMF solvent molecule (calculated 11.6%) and the final weight loss from 300 °C corresponds to the decomposition of the compound. The above results reveal satisfactory thermal stabilities of as-prepared Ni-MOFs.

The nitrogen-enriched conjugated ligands could bestow MOFs with an attractive conductivity, and therefore, a four-probe method with pressed pellets has been adopted to evaluate the intrinsic electrical conductivity of Ni-BPE which is 4×10^{-3} S m^{-1} (Fig. 2e). After replacing the BPE ligand with the more π-conjugated BPA ligand, encouragingly, the conductivity of Ni-BPA increases up to 5.64×10^{-3} S m^{-1}, which is 40% higher than that of Ni-BPE. The improved conductivity brought by the ligand delocalization expansion strategy was further verified by density functional theory (DFT) calculations. Fig. 2c and d show the constructed models of Ni-BPE and Ni-BPA for calculation. According to Fig. 2f, the density of states (DOS) near the Fermi level is continuously distributed, and thus Ni-BPE and Ni-BPA are all in metallic states.[55] Notably, near the Fermi level, Ni-BPA has a higher DOS than Ni-BPE, suggesting that Ni-BPA possesses a much higher carrier concentration and electrical conductivity than Ni-BPE,[55,56] which is consistent with the conductivity measured by the four-probe method.

In view of the enhanced electronic conductivity, the microstructure and morphology of Ni-BPA and Ni-BPE were

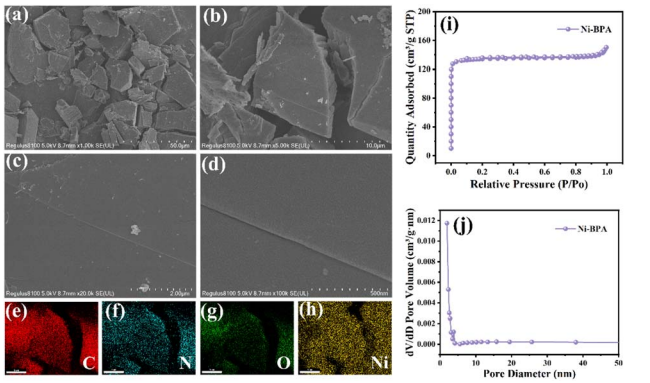

Fig. 3 The SEM images in different dimension scales of 50 μm (a), 10 μm (b), 2 μm (c) and 500 nm (d) in Ni-BPA. The EDS mapping of C (e), N (f), O (g) and Ni (h) elements in Ni-BPA. The N_2 adsorption/desorption isotherms (i) and aperture distribution (j) of Ni-BPA.

characterized by using scanning electron microscopy (SEM) at various magnifications. As illustrated in Fig. 3a–d and S3a–d,† Ni-BPA and Ni-BPE present irregular block shaped structures with a length and width of approximately 8 × 10 μm. Interestingly, the crystal surface of Ni-BPE reveals a rough fish scale like appearance, while Ni-BPA is relatively smooth and has subtle protrusions and indentations. Moreover, the energy-dispersive spectroscopy (EDS) elemental mapping images of Ni-BPA (Fig. 3e–h) and Ni-BPE (Fig. S3e–h†) unveil the uniform distribution of C, N, O and Ni elements throughout the structure, indicating that Ni(II) ions have been successfully coordinated with organic linkers. Subsequently, N_2 adsorption/desorption isotherms at 77 K were obtained to evaluate the actual specific surface areas and porosities of Ni-BPA and Ni-BPE (Fig. 3i, j and S3i, j†). Significantly, Ni-BPA displays a higher specific surface area (550.872 m^2 g^{-1}) and a smaller average pore diameter (6.546 nm) than Ni-BPE (74.059 m^2 g^{-1} and 12.172 nm), which may be due to the exchange of rigid ligands. BPA with a carbon–carbon triple bond has superior linear rigidity and configurational stability, facilitating the formation of highly ordered microporous frameworks, thereby enhancing effective surface area. In contrast, the pliability of BPE with a double bond may induce local framework distortion, compromise pore regularity and ultimately diminish specific surface area.

Electrochemical performance

The supercapacitor performances of as-prepared Ni-BPE and Ni-BPA samples were evaluated under a three-electrode system. As shown in Fig. 4a, the cyclic voltammetry (CV) curves at 30 mV s^{-1} within the operating potential range of 0–0.6 V reveal the faradaic reaction kinetics occurring in the samples. Compared to Ni-BPE, obviously, Ni-BPA has a larger integral area of the CV curve, suggesting better specific capacitance and kinetics reversibility under the same conditions.[57] Two pairs of similar CV curves with distinct redox peaks of Ni-MOFs electrodes have also been observed, which originated from the change in valence states of Ni^{2+}/Ni^{3+} ions in the presence of OH^- ions. The shape of CV curves is nearly maintained at various scan rates

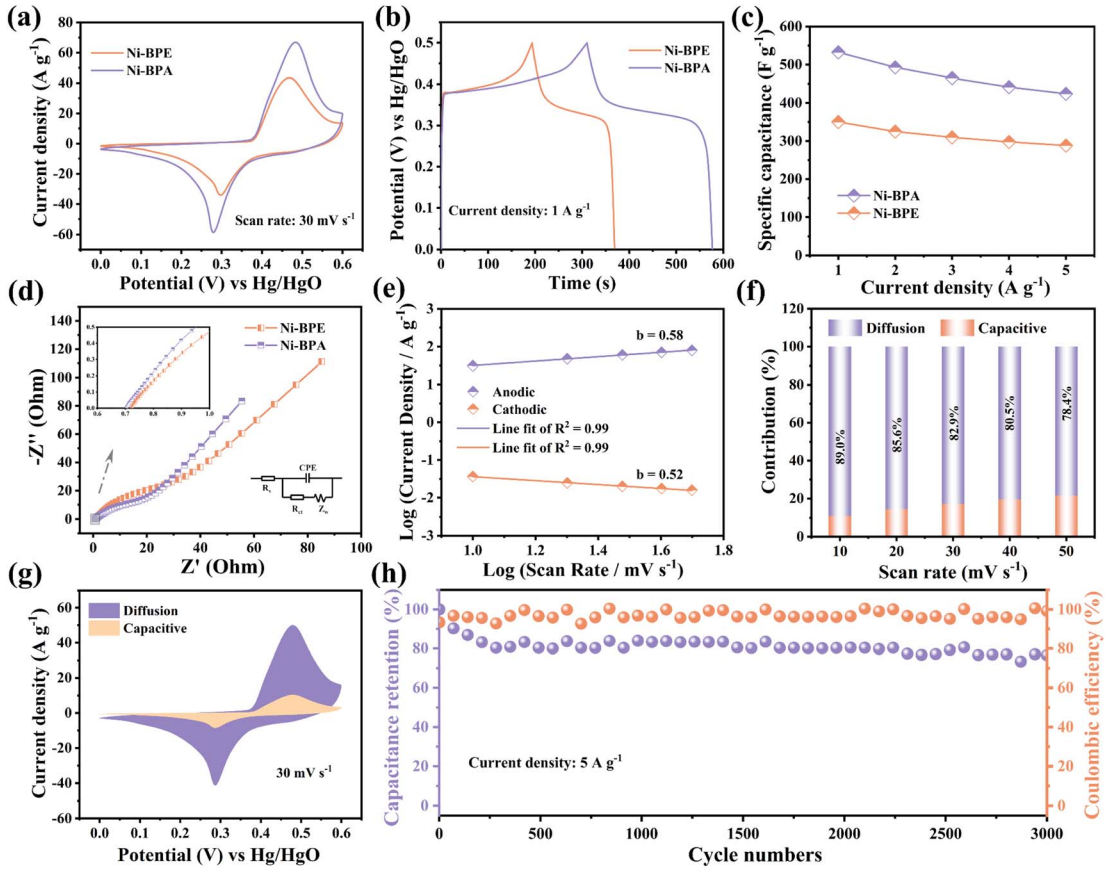

Fig. 4 (a) CV curves, (b) GCD curves, (c) specific capacities at various current densities and (d) Nyquist plots (inset shows the circuit diagram) of the compounds. (e) Logarithm peak current *versus* logarithm scan rate plots, (f) capacitive and diffusion contribution for charge storage, (g) capacitive and diffusion contribution at a scan rate of 30 mV s^{-1} and (h) cycling performance at 5 A g^{-1} of Ni-BPA.

from 10 to 50 mV s^{-1} (Fig. S4a and c†), indicative of the highly reversible redox reactions.[58] In order to better understand the energy storage capabilities of compounds, the galvanostatic charge/discharge (GCD) tests were carried out. As depicted in Fig. 4b, the nonlinear constant current discharge curves support the pseudocapacitive nature of two electrodes and at the same current density of 1 A g^{-1}, Ni-BPA displays significant discharge time compared the isostructural Ni-BPE, indicating that it has better specific capacitance.[59] Based on formula (S1),† when the current density is 1 A g^{-1}, the determined specific capacitance for Ni-BPE is 350.0 F g^{-1}. The optimal Ni-BPA shows a specific capacitance of 532.4 F g^{-1}, which prominently increases to 1.52 times that of Ni-BPE, exceeding the values of some other MOF-based materials (Table S4†). The increase in specific capacitance may be generated from superior electron transfer ability of BPA-containing Ni-MOFs. As the current densities increase to 5 A g^{-1}, the specific capacitance of Ni-BPE and Ni-BPA decreases to 288.0 F g^{-1} and 424.0 F g^{-1}, respectively (Fig. 4c), which are due to insufficient time for interaction of OH^- ions with electrode materials. It is noteworthy that the discharge plateaus remain similar during the processes of increasing current densities, representing stability of Ni-BPE and Ni-BPA electrodes (Fig. S4b and d†).

To get insight into the charge transport properties, the electrochemical impedance spectroscopy (EIS) tests of the Ni-BPE and Ni-BPA modified electrodes were conducted in the frequency range of 0.1 Hz to 100 kHz. According to the Nyquist plots (Fig. 4d), when compared to BPE-containing frameworks, Ni-BPA displays a smaller intercept of the *x*-axis and smaller radius of an arc. The intercept of the *x*-axis refers to solution resistance (R_s) containing resistance of the electrolyte and the contact resistance at the electrode interface, and the radius of an arc represents charge transfer resistance (R_{ct}).[60] The lower R_s (0.68 Ω) and R_{ct} (24.8 Ω) in the high-frequency region and the steeper linear gradient in the low-frequency region signify a faster charge transfer rate and more effective ion diffusion efficiency of the Ni-BPA electrode. These feedbacks further demonstrate that crystal engineering is an effective strategy to boost the charge–discharge efficiency of MOF electrodes. Furthermore, the optimized Ni-BPA-based supercapacitor retains 77.0% of its initial capacitance and 99.1% coulombic efficiency over 3000 charge–discharge cycles at 5 A g^{-1} (Fig. 4h). Remarkably, even after 4000 charge–discharge cycles at 7 A g^{-1}, it can maintain 75.3% capacitance retention and 99.3% coulombic efficiency (Fig. S5†), confirming the durable cycling stability.

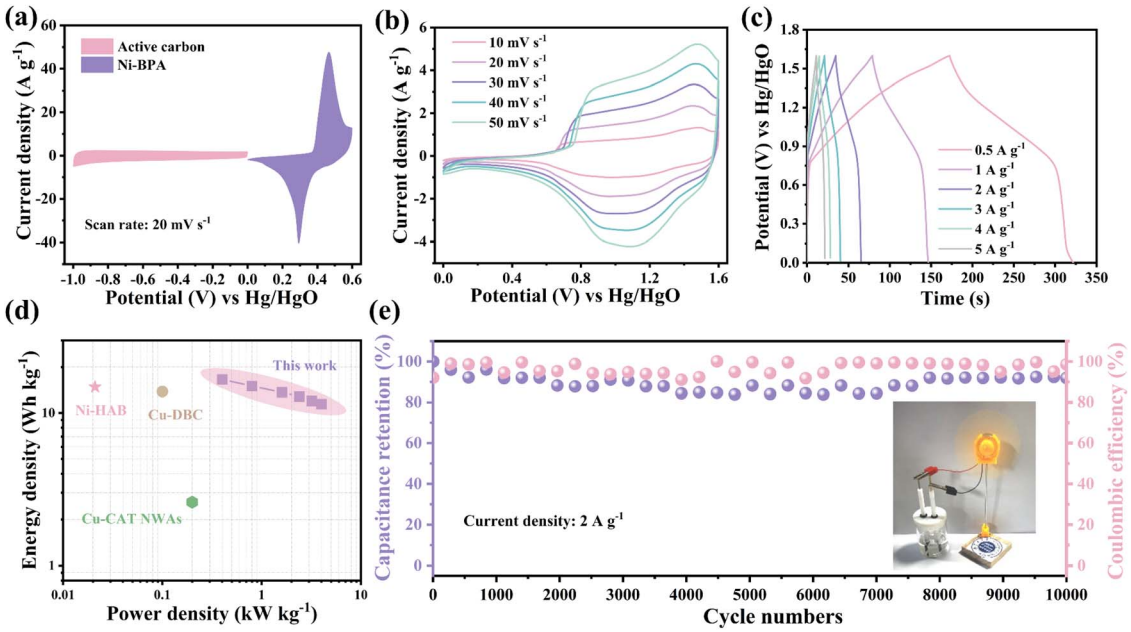

Fig. 5 (a) CV curves. (b) CV curves at various scan rates from 10 to 50 mV s^{-1}, (c) GCD curves at various current densities from 0.5 to 5 A g^{-1}, (d) Ragone plot and (e) cycling performance (inset shows a small fan) of the Ni-BPA//AC device.

In order to conduct in-depth research on the charge storage mechanism, the relationship between the logarithm peak current (i) and logarithm scan rate (v) was presented according to the power law of $\log i = b \log v + \log a$ (a and b are adjustable parameters).[61] In general, if b is close to 0.5, the diffusion-controlled process (C_{dl}) mainly controls the charge storage and if b is close to 1, the charge storage is mainly controlled by the capacitive-control process (C_p). The fitted b values for anodic and cathodic peaks of Ni-BPE are found to be 0.64 and 0.61 (Fig. S7†), and the fitted b values of Ni-BPA are 0.58 and 0.52 (Fig. 4e), which imply that C_{dl} primarily plays a role in the charge storage process of Ni-BPE and Ni-BPA. Moreover, the capacitance contribution was determined by using the equation $i = k_1v + k_2v^{1/2}$, in which k_1v = capacitive-control contribution and $k_2v^{1/2}$ = diffusion-controlled contribution.[62] The diffusion contributions of Ni-BPE decrease from 79.8 to 63.8% (Fig. S8†) and the diffusion contributions of Ni-BPA decrease from 89.0 to 78.4% (Fig. 4f, g and S6†) as the scan rate gradually increases from 10 to 50 mV s^{-1}, which suggest the dominance of the C_{dl} over the total capacitance contributions.

Encouraged by the preferable electrochemical performance of the Ni-BPA electrode, an asymmetric supercapacitor (ASC) device, Ni-BPA//AC, utilizing Ni-BPA as the positive electrode and activated carbon (AC) as the negative electrode was fabricated to explore the practical application, in which the ideal mass ratio of Ni-BPA and AC is calculated by using eqn (S2).† The possible potential voltage for the Ni-BPA//AC ASC device is 0–1.6 V on the basis of the CV curves at a scan rate of 20 mV s^{-1} of Ni-BPA (0–0.6 V) and AC (−1.0–0 V) (Fig. 5a). As depicted in Fig. S9a,† the CV curves exhibit distortion in the potential window of 0–1.7 V. Thus, the optimal operational voltage range is 0–1.6 V. At the scan rates from 10 to 50 mV s^{-1}, the CV curves of Ni-BPA//AC presented similar redox peaks (Fig. 5b), suggesting excellent electrochemical reversibility and rate performance. Meanwhile, the calculated specific capacitances of Ni-BPA//AC are 46.7, 42.2, 38.4, 36.0, 33.8 and 32.2 F g^{-1}, respectively (Fig. 5c and S9b†), at current densities ranging from 0.5 to 5 A g^{-1}. Furthermore, according to eqn (S3) and (S4),† the power density and energy density were calculated and are displayed in Ragone plots (Fig. 5d), in which the ASC device demonstrates a maximum energy density of 16.6 W h kg^{-1} at a power density of 400 W kg^{-1} and a maximum power density of 4000 W kg^{-1} at an energy density of 11.4 W h kg^{-1}. Ni-BPA//AC delivered comparable energy density to those of many MOF-based ASC devices like Cu-DBC (13.8 W h kg^{-1} at 100 W kg^{-1}),[63] Cu-CAT NWAs (2.6 W h kg^{-1} at 200 W kg^{-1}),[64] Ni-HAB (14.8 W h kg^{-1} at 21 W kg^{-1}),[65] *etc.* Importantly, the Ni-BPA//AC device maintained excellent durability with a high capacitance retention of 91.9% and an outstanding coulombic efficiency of 98.6% after 10 000 cycles at 2 A g^{-1} (Fig. 5e). Impressively, the high capacitance retention of Ni-BPA//AC is better than that of these MOF-based ASC devices reported (Table S5†). Encouragingly, the Ni-BPA//AC device possesses potential application in the field of energy storage, and can power a small fan (Fig. 5e).

Conclusions

In summary, two new 3D Ni-based conductive MOFs with a 2-fold interpenetrating structure were well-designed and synthesized by adopting the conjugated nitrogen-rich ligands. Ni^{2+} ions bridge H_3L and BPE containing a vinyl group or BPA containing an ethynyl group, enabling electrons to delocalize through the extended π-conjugation of the ligands, resulting in excellent electronic conductivity of MOFs. Moreover, based on experimental results and a DFT study, we have also proven that rational crystal engineering that involves upgrading the local

conjugation in frameworks is an effective strategy to endow MOFs with improved conductivity and promising electrochemical performance. The resulting Ni-BPA material exhibited a satisfactory specific capacitance of 532.4 F g^{-1} and an asymmetric supercapacitor maintained a high capacitance retention of 91.9% after 10 000 cycles. This work has enriched the nitrogenous 3D conductive MOF family and provided new insights for the future assembly of 3D conductive MOFs.

Data availability

All experimental and computational data and methods related to this study can be found in the text and ESI.†

Author contributions

H. Tai: conceptualization, investigation, synthesis, data curation, writing – original draft. X. Zhang: methodology, characterization analysis. Y. Rong: formal analysis, electrochemical measurements. Z. Liu: resources, supervision, writing – review & editing.

Conflicts of interest

There are no conflicts to declare.

Acknowledgements

We are grateful for the financial support provided by the NSFC (22261038).

Notes and references

1 M. A. Gaidimas, C. S. Smoljan, Z. Ye, C. L. Stern, C. D. Malliakas, K. O. Kirlikovali and O. K. Farha, *Chem. Sci.*, 2025, **16**, 3895–3903.
2 Z. Lv, R. Lin, Y. Yang, K. Lan, C. Hung, P. Zhang, J. Wang, W. Zhou, Z. Zhao, Z. Wang, J. Zou, T. Wang, T. Zhao, Y. Xu, D. Chao, W. Tan, B. Yan, Q. Li, D. Zhao and X. Li, *Nat. Chem.*, 2025, **17**, 177–185.
3 X. Li, X. Su, T. Su, L. Chen and Z. Su, *Chem. Sci.*, 2025, **16**, 5353–5368.
4 H. Woo, A. M. Devlin and A. J. Matzger, *J. Am. Chem. Soc.*, 2023, **145**, 18634–18641.
5 T. Chen, Z. Deng, W. Lu, M. Lu, J. Xu, F. Mao, C. Li, C. Zhang and K. Wang, *Inorg. Chem.*, 2024, **63**, 18699–18709.
6 S. Naskar, D. Fan, A. Ghoufi and G. Maurin, *Chem. Sci.*, 2023, **14**, 10435–10445.
7 X. Xie, Z. Zhang, Q. Cao, Y. Huang, D. Luo, H. Zeng, W. Lu and D. Li, *J. Am. Chem. Soc.*, 2024, **146**, 30155–30163.
8 W. Zhang, G. Tan, J. Hu, Q. Wang, W. Yan and Q. Man, *Chem. Eng. J.*, 2023, **478**, 147414.
9 X. Wang, X. Zhang, A. He, J. Guo and Z. Liu, *Inorg. Chem.*, 2024, **63**, 6948–6956.
10 D. Sengupta, S. Bose, X. Wang, N. M. Schweitzer, C. D. Malliakas, H. Xie, J. Duncan, K. O. Kirlikovali, T. Yildirim and O. K. Farha, *J. Am. Chem. Soc.*, 2024, **146**, 27006–27013.
11 X. Yao, D. Cui, C. Zhu, J. He, F. Meng, S. Yang, M. Dong, G. Shan, M. Zhang, C. Sun, X. Wang and Z. Su, *ACS Mater. Lett.*, 2024, **6**, 5112–5119.
12 P. Gupta, B. Rana, R. Maurya, R. Kalita, M. Chauhan and K. Manna, *Chem. Sci.*, 2025, **16**, 2785–2795.
13 J. Chen, M. Li, R. Sun, Y. Xie, J. R. Reimers and L. Sun, *Adv. Funct. Mater.*, 2024, **34**, 2315276.
14 J. Zhang, Y. Gao, L. Song and H. Hong, *J. Mol. Struct.*, 2025, **1328**, 141321.
15 Y. Zhang, Y. Wei, Y. Li, F. Huang, J. Pan, S. Chen, P. Wu, Y. Wang and J. Wang, *Inorg. Chem.*, 2025, **64**, 5140–5148.
16 S. Wang, S. Wang, X. Guo, Z. Wang, F. Mao, L. Su, H. Wu, K. Wang and Q. Zhang, *Inorg. Chem. Front.*, 2021, **8**, 4878.
17 S. Khan, S. Chand, P. Sivasakthi, P. K. Samanta and C. Chakraborty, *Small*, 2024, **20**, 2401102.
18 Y. Yan, X. Lin, J. Ge and X. Li, *Chem. Eng. J.*, 2023, **468**, 143739.
19 A. A. Talin, A. Centrone, A. C. Ford, M. E. Foster, V. Stavila, P. Haney, R. A. Kinney, V. Szalai, F. El Gabaly, H. P. Yoon, F. Léonard and M. D. Allendorf, *Science*, 2014, **343**, 66–69.
20 K. Wang, Q. Li, Z. Ren, C. Li, Y. Chu, Z. Wang, M. Zhang, H. Wu and Q. Zhang, *Small*, 2020, **16**, 2001987.
21 R. Saha, K. Gupta and C. J. G. García, *Cryst. Growth Des.*, 2024, **24**, 2235–2265.
22 S. Shin, J. W. Gittins, C. J. Balhatchet, A. Walsh and A. C. Forse, *Adv. Funct. Mater.*, 2023, **34**, 2308497.
23 T. K. Ghosh and G. R. Rao, *Dalton Trans.*, 2023, **52**, 5943–5955.
24 G. Xu, C. Zhu and G. Gao, *Small*, 2022, **18**, 2203140.
25 J. Yang, J. Wang, C. Lou, Y. Cui, X. Huang, H. Yu, L. Bai, W. Wang, X. Zhang and H. Pan, *J. Mol. Struct.*, 2024, **1311**, 138392.
26 T. Wang, J. Lei, Y. Wang, L. Pang, F. Pan, K. Chen and H. Wang, *Small*, 2022, **18**, 2203307.
27 M. A. Saghafizadeh, A. M. Zardkhoshoui and S. S. H. Davarani, *Chem. Eng. J.*, 2025, **508**, 160817.
28 H. Gong, M. Yue, F. Xue, S. Zhang, M. Ma, X. Mu, H. Xue and R. Ma, *Adv. Funct. Mater.*, 2024, **35**, 2411854.
29 L. Niu, T. Wu, M. Chen, L. Yang, J. Yang, Z. Wang, A. A. Kornyshev, H. Jiang, S. Bi and G. Feng, *Adv. Mater.*, 2022, **34**, 2200999.
30 S. Zhou, T. Liu, M. Strømme and C. Xu, *Angew. Chem., Int. Ed.*, 2024, **63**, e202318387.
31 J. Zhao, T. Zhang, J. Ren, Z. Zhao, X. Su, W. Chen and L. Chen, *Chem. Commun.*, 2023, **59**, 2978–2981.
32 C. Chen, C. Yang, X. Fu, Y. Yang, S. Huang, J. Hou, M. Yang, Y. Su and X. Zhuang, *J. Mater. Chem. A*, 2024, **12**, 29606–29614.
33 C. Huang, W. Sun, Y. Jin, Q. Guo, D. Mücke, X. Chu, Z. Liao, N. Chandrasekhar, X. Huang, Y. Lu, G. Chen, M. Wang, J. Liu, G. Zhang, M. Yu, H. Qi, U. Kaiser, G. Xu, X. Feng and R. Dong, *Angew. Chem., Int. Ed.*, 2024, **63**, e202313591.
34 J. Y. Choi, J. Flood, M. Stodolka, H. T. B. Pham and J. Park, *ACS Nano*, 2022, **16**, 3145–3151.

35 L. Lin, C. Zhang, L. Yin, Y. Sun, D. Xing, Y. Liu, P. Wang, Z. Wang, Z. Zheng, H. Cheng, Y. Dai and B. Huang, *Small*, 2024, **20**, 2309256.
36 K. Wang, S. Wang, J. Liu, Y. Guo, F. Mao, H. Wu and Q. Zhang, *ACS Appl. Mater. Interfaces*, 2021, **13**, 15315–15323.
37 S. Mishra, M. K. Singh, D. Pandey, D. K. Rai and A. Raghuvanshi, *J. Mater. Chem. A*, 2024, **12**, 4534–4543.
38 M. Shahbaz, S. Sharif, M. W. Mushtaq, Z. Ghaznazvi, Z. Iqbal, M. A. Khurshid, O. Şahin, S. Shahzad, M. Saeed and A. Shahzad, *J. Mater. Chem. A*, 2025, **13**, 6524–6538.
39 M. I. Anwar, M. Asad, L. Ma, W. Zhang, A. Abbas, M. Y. Khan, M. Zeeshan, A. Khatoon, R. Gao, S. Manzoor, M. Naeem Ashiq, S. Hussain, M. Shahid and G. Yang, *Coord. Chem. Rev.*, 2023, **478**, 214967.
40 C. Wu, P. Geng, G. Zhang, X. Li and H. Pang, *Small*, 2024, **20**, 2308264.
41 J. Perego, C. X. Bezuidenhout, I. Villa, F. Cova, R. Crapanzano, I. Frank, F. Pagano, N. Kratochwill, E. Auffray, S. Bracco, A. Vedda, C. Dujardin, P. E. Sozzani, F. Meinardi, A. Comotti and A. Monguzzi, *Nat. Commun.*, 2022, **13**, 3504.
42 K. Wu, X. Liu, P. Cheng, Y. Huang, J. Zheng, M. Xie, W. Lu and D. Li, *J. Am. Chem. Soc.*, 2023, **145**, 18931–18938.
43 Y. Pan, J. Wang, S. Chen, W. Yang, C. Ding, A. Waseem and H. Jiang, *Chem. Sci.*, 2022, **13**, 6696–6703.
44 H. Liu, S. Zhao, Q. Li, X. Li, Y. He, P. Liu, Y. Wang and J. Li, *J. Mater. Chem. A*, 2024, **12**, 9527–9531.
45 N. Huang, B. Chu, D. Chen, B. Shao, Y. Zheng, L. Li, X. Xiao and Q. Xu, *J. Am. Chem. Soc.*, 2025, **147**, 8832–8840.
46 D. Sheberla, J. C. Bachman, J. S. Elias, C. Sun, Y. Shao-Horn and M. Dincă, *Nat. Mater.*, 2017, **16**, 220–224.
47 X. Hang, X. Wang, J. Chen, M. Du, Y. Sun, Y. Li and H. Pang, *Inorg. Chem.*, 2025, **64**, 427–434.
48 G. M. Sheldrick, *Acta Crystallogr., Sect. A: Found. Adv.*, 2015, **71**, 3–8.
49 G. Kresse and J. Furthmüller, *Phys. Rev. B: Condens. Matter Mater. Phys.*, 1996, **54**, 11169–11186.
50 J. P. Perdew, K. Burke and M. Ernzerhof, *Phys. Rev. Lett.*, 1996, **77**, 3865–3868.
51 S. Grimme, J. Antony, S. Ehrlich and H. Krieg, *J. Chem. Phys.*, 2010, **132**, 154104.
52 S. Grimme, S. Ehrlich and L. Goerigk, *J. Comput. Chem.*, 2011, **32**, 1456–1465.
53 K. Momma and F. Izumi, *J. Appl. Crystallogr.*, 2011, **44**, 1272–1276.
54 X. Yang, Y. Yan, W. Wang, Z. Hao, W. Zhang, W. Huang and Y. Wang, *Inorg. Chem.*, 2021, **60**, 3156–3164.
55 Y. Ji, W. Li, Y. You and G. Xu, *Chem. Eng. J.*, 2024, **496**, 154009.
56 Z. Xia, X. Jia, X. Ge, C. Ren, Q. Yang, J. Hu, Z. Chen, J. Han, G. Xie, S. Chen and S. Gao, *Angew. Chem., Int. Ed.*, 2021, **60**, 10228–10238.
57 L. Pang, Y. Lei, Y. Zou, F. Yu, F. Feng, J. Lu, W. Pang, Z. Liu, P. Liu, A. P. O' Mullane, G. Wang and H. Wang, *Chem. Eng. J.*, 2024, **500**, 157470.
58 H. Ding, Z. Liu, J. Xie, Z. Shen, D. Yu, Y. Chen, Y. Lu, H. Zhou, G. Zhang and H. Pang, *Angew. Chem., Int. Ed.*, 2024, **63**, e202410255.
59 M. R. Pallavolu, A. N. Banerjee, N. Roy, D. Merum, J. Nallapureddy and S. W. Joo, *Chem. Eng. J.*, 2024, **498**, 155240.
60 Z. Li, H. Mi, F. Guo, C. Ji, S. He, H. Li and J. Qiu, *Inorg. Chem.*, 2021, **60**, 12197–12205.
61 Y. Lu, G. Zhang, H. Zhou, S. Cao, Y. Zhang, S. Wang and H. Pang, *Angew. Chem., Int. Ed.*, 2023, **62**, e202311075.
62 A. Lakshmi-Narayana, N. Attarzadeh, V. Shutthanandan and C. V. Ramana, *Adv. Funct. Mater.*, 2024, **34**, 2316379.
63 J. Liu, Y. Zhou, Z. Xie, Y. Li, Y. Liu, J. Sun, Y. Ma, O. Terasaki and L. Chen, *Angew. Chem., Int. Ed.*, 2020, **59**, 1081–1086.
64 W. Li, K. Ding, H. Tian, M. Yao, B. Nath, W. Deng, Y. Wang and G. Xu, *Adv. Funct. Mater.*, 2017, **27**, 1702067.
65 D. Feng, T. Lei, M. R. Lukatskaya, J. Park, Z. Huang, M. Lee, L. Shaw, S. Chen, A. A. Yakovenko, A. Kulkarni, J. Xiao, K. Fredrickson, J. B. Tok, X. Zou, Y. Cui and Z. Bao, *Nat. Energy*, 2018, **3**, 30–36.